Improved progressive TIN densification filtering algorithm for airborne LiDAR data in forested areas

XiaoqianZhao[a,b], Qinghua Guo[a,c,*], YanjunSu[c], and BaolinXue[a]

[a]*State Key Laboratory of Vegetation and Environmental Change, Institute of Botany, Chinese Academy of Sciences, Beijing 100093, China;Tel.: +86-010-62836591; E-mail: zhaoxiaoqian@ibcas.ac.cn (X.Z.); xuebaolin@ibcas.ac.cn (B.X.)*

[b]*University of Chinese Academy of Sciences, No.19A Yuquan Road, Beijing 100049, China*

[c]*Sierra Nevada Research Institute, School of Engineering, University of California at Merced,Merced, CA 95343, USA;Tel.: +1(209)761-6824; E-mail: ysu3@ucmerced.edu (Y.S.)*

[*]Corresponding author: Qinghua Guo; Tel.: +86-10-62836157;

E-mail: guo.qinghua@gmail.com

Improved progressive TIN densification filtering algorithm for airborne LiDAR data in forested areas

Abstract

Filtering of light detection and ranging (LiDAR) data into the ground and non-ground points is a fundamental step in processing raw airborne LiDAR data. This paper proposes an improved progressive triangulated irregular network (TIN) densification (IPTD) filtering algorithm that can cope with a variety of forested landscapes, particularly both topographically and environmentally complex regions. The IPTD filtering algorithm consists of three steps: 1) acquiring potential ground seed points using the morphological method; 2) obtaining accurate ground seed points; and 3) building a TIN-based model and iteratively densifying TIN. The IPTD filtering algorithm was tested in 15 forested sites with various terrains (i.e., elevation and slope) and vegetation conditions (i.e., canopy cover and tree height), and was compared with seven other commonly used filtering algorithms (including morphology-based, slope-based, and interpolation-based filtering algorithms). Results show that the IPTD achieves the highest filtering accuracy for nine of the 15 sites. In general, it outperforms the other filtering algorithms, yielding the lowest average total error of 3.15% and the highest average kappa coefficient of 89.53%.

Keywords: light detection and ranging; ground filtering; ground points; triangulated irregular network; digital terrain model.

Abbreviations:

LiDAR, Light Detection and Ranging;

TIN, Triangulated Irregular Network;

PTD, Progressive triangulated irregular network densification;

IPTD, Improved Progressive triangulated irregular network densification;

DTM, Digital Terrain Model;

CHM, Canopy Height Model;

TI, Type I errors;

TII, Type II errors;

TE, total errors;

kp, kappa coefficient;

1. Introduction

Light detection and ranging (LiDAR) data are widely used in forest inventory and management, and forest ecosystem investigations (Wulder et al., 2008; Müller et al., 2010; Korhonen et al., 2011; Vauhkonen et al., 2014). In forestry applications, distinguishing ground points from non-ground points is a preliminary but essential step in processing raw LiDAR data (Nord-Larsen and Riis-Nielsen, 2010; Maltamo et al., 2014). Algorithms for extracting bare earth from airborne LiDAR data have become more and more advanced and automatic (Axelsson, 2000; Zhang et al., 2003; Silván-Cárdenas and Wang, 2006; Mongus and Žalik, 2012; Susaki, 2012; Pingel et al., 2013). However, most of these filtering algorithms work well only on relatively flat and low-vegetated regions. Filtering in areas with highly rugged terrain, steep slopes, dense vegetation, and terrain discontinuities is still a challenge (Pingel et al., 2013). Moreover, existing filtering algorithms were usually tested on specific sites, and their adaptability to different forestry landscapes is still uncertain. Therefore, it is crucial to develop a filtering algorithm that can cope with various forested landscapes, especially for topographically and environmentally complex regions.

Generally, existing filtering algorithms can be classified into different categories based on the filtering methodology (Liu, 2008; Meng et al., 2010), i.e., slope (Vosselman, 2000; Sithole, 2001; Susaki, 2012), interpolation (Kraus and Pfeifer, 1998; Axelsson, 2000; and Evans Hudak, 2007; Kobler et al., 2007; Mongus and Žalik, 2012; Hu et al., 2014), morphology (Zhang et al., 2003; Chen et al., 2007; Li, 2013; Pingel et al., 2013), and segmentation (Sithole and Vosselman, 2005; Zhang and

Lin, 2013) filters. We provide a concise review of the morphology and progressive triangulated irregular network (TIN) densification (PTD) filters, because they are closely linked to the proposed algorithm.

Morphological filtering algorithms are based on morphological operations such as opening and closing, and work on rasterized point clouds (Zhang et al., 2003; Najman and Talbot, 2010). Zhang et al. (2003) used successively increasing window sizes to process the raster data. If the elevation difference between the original raster data and the data after the opening operation was higher than a threshold, the grid was labeled as a non-ground grid. This process was iterated with increasing window sizes until the window size was greater than the maximum object size. Chen et al. (2007) considered elevation changes without the constant-slope constriction. The morphological opening with a fixed window size was used to remove most vegetation points. Then, the morphological opening operator with increasing window sizes was used to remove buildings. Possible building regions were detected by calculating height differences using data before and after the morphological opening operation. Elevations on the boundaries of possible building regions were analyzed and compared with a combination of parameters, such as percentiles, to determine whether the region contained buildings. For vegetation areas, this method cannot remove all vegetation points. Pingel et al. (2013) improved the morphological method simply by changing the window size linearly instead of exponentially, providing painting technique to interpolate empty cells and digital terrain model (DTM), and changing the elevation threshold to identify the classifications of points. However, for

all these morphological filtering algorithms, defining the window size requires prior knowledge of the sizes of the contained objects, and the conversion from LiDAR points to raster images may reduce the filtering precision. The unavoidable issues associated with the morphological algorithms make it hard to remove non-ground points while retaining the terrain details (Liu, 2008).

Progressive densification is a method that builds an initial DTM from certain initial ground seed points, and then progressively adds more points from the unclassified points to the DTM based on certain criteria, e.g. the distance between the point and the DTM (Axelsson, 2000). PTD has gained popularity, not only because of its robustness and effectiveness in extracting ground points, but also owing to its integration in the commercial softwareTerrascan™<http://www.terrasolid.com/products/terrascanpage.php>. However, PTD has deficiencies when dealing with discontinuities, edges, and steep hills (Lin and Zhang, 2014) and tends to remove ground points on steep hills and flatten the terrain.

To obtain better filtering performance for complex forested sites, we proposed improved PTD (IPTD) filtering algorithm by combining it with a morphological method. Compared with previous work, the enhancements of the proposed algorithm focus on three aspects. (1) Ground seed points are acquired through a morphological opening operation instead of using the lowest points in user-defined grids. This method provides more ground seed points that are almost evenly distributed in general. (2) The simulated ground points along the buffer zone participate in the original

TIN-based DTM construction to improve the quality of TIN avoiding the formation of unsuitable triangles. (3) Downward densification is performed before upward densification to improve the ability of the IPTD in dealing with slope variations. We expect that the IPTD would be a useful tool in airborne LiDAR data application, especially for mountainous forested areas.

2. Data

2.1. Study area

We chose Providence, San Joaquin Range, Wolverton and Tokopah, and Courtwright Road, situated in the Southern Sierra Nevada Mountains, California, USA, as our study areas (Fig. 1). The primary tree species within these areas, which are dominated by mixed conifers, include, in the order of abundance, white fir (*Abies concolor*), ponderosa pine (*Pinus ponderosa*), incense cedar (*Calocedrus decurrens*), sugar pine (*Pinus lambertiana*), and giant sequoia (*Sequoiadendron giganteum*), together with black oak (*Quercus kelloggii*) and canyon live oak (*Quercus chrysolepis*).

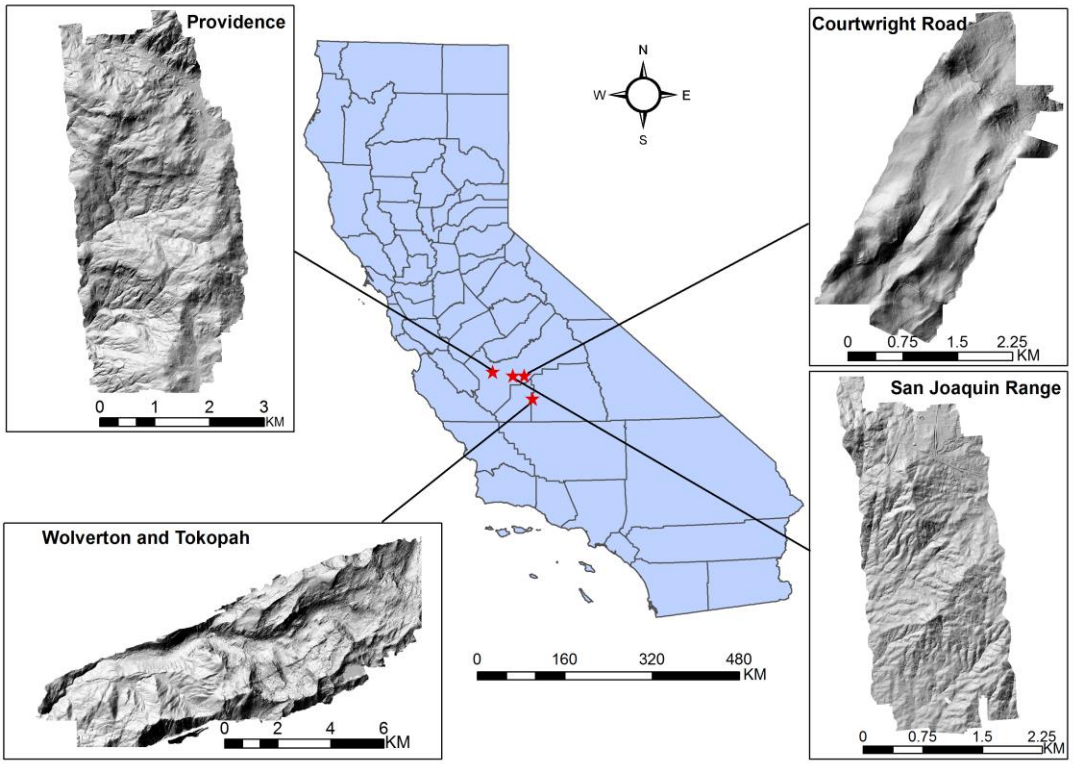

Fig.1. Study areas in Southern Sierra Nevada, California, USA.

We selected 15 500 × 500 m sites from the four study areas. Sites 1 and 2 are located in Providence; sites 4–7 are located in the San Joaquin Range; site 8 is located in Wolverton and Tokopah; and the remaining sites are located in Courtwright Road. Statistics of the vegetation conditions and terrain for each site are given in Table 1. These statistics were calculated from LiDAR data using the software ESRI™ ArcGIS. The 30 m pixel-level canopy cover for each study site was calculated from the LiDAR data using a method based on canopy height model (CHM) (Lucas et al., 2006). We first generated a 1 m resolution CHM from LiDAR point clouds. Then, the canopy cover of each 30 m grid cell was calculated as the percentage of the 1 m pixels with heights higher than a threshold (i.e., 1.5 m in this study). These study sites contain various topographic conditions with the mean elevation changing from below 450 m to over 3000 m and the mean slope changing from flat (below 10°) to precipitous

142 (over 40°). Moreover, the vegetation conditions vary greatly. The mean canopy cover
143 changes from less than 20% to 90%, and mean tree height ranges between about 5 m
144 and 20 m.

Table 1

Statistics and description of each site in the study areas.

Site	Elevation (m)				Tree height (m)				Canopy cover (%)				Slope (°)				Return numbers[d]				Mean density (pts/m^2)
	Min[a]	Max[b]	Mean	SD[c]	Min[a]	Max[b]	Mean	SD[c]	Min[a]	Max[b]	Mean	SD[c]	Min[a]	Max[b]	Mean	SD[c]	First return	Second return	Third return	Fourth return	
1	2590	2728	2671	31	3.8	25.1	10.3	4.8	0	88	30	19	0.0	65.5	17.1	7.0	2146134	33071	99084	16085	10.4
2	2693	2724	2703	5	5.3	21.5	13.1	2.9	13	80	51	12	0.0	53.7	6.0	3.7	2199586	580102	187179	29361	12.0
3	1482	1697	1562	46	8.3	36.5	20.6	4.4	50	100	90	9	0.2	65.6	21.9	8.4	2235338	955957	291156	51983	14.1
4	1478	1690	1577	41	7.8	41.4	22.3	5.8	51	100	89	9	0.1	60.4	21.2	8.8	2140121	984314	317423	60752	14.0
5	1898	1978	1949	19	4.3	33.1	16.9	4.7	8	100	68	18	0.0	74.6	13.2	7.6	2132490	589664	166448	28952	11.7
6	1908	1993	1960	19	4.0	27.7	13.7	5.3	2	94	54	21	0.0	71.8	12.4	7.1	2112343	535531	157248	27402	11.3
7	415	442	426	6	3.8	13.6	6.2	1.8	0	86	24	18	0.0	52.0	7.1	4.4	2208498	452116	106759	10104	11.1
8	2250	2465	2358	54	3.9	39.2	20.6	7.4	0	94	59	22	0.2	72.7	25.9	8.1	1947854	586216	180680	30656	11.0
9	2672	3014	2829	85	4.7	29.0	15.4	5.6	13	92	55	18	1.6	77.7	31.4	6.5	2215154	562225	151063	22124	11.8
10	2800	3213	3041	106	3.9	25.3	5.3	1.9	0	91	17	17	0.3	88.3	36.1	14.0	2088055	35276	4185	285	8.5
11	2090	2468	2251	90	4.3	39.7	16.7	6.9	3	97	57	20	0.1	80.6	33.3	9.9	2292499	551141	152094	23973	12.1
12	2176	2727	2446	145	3.9	30.8	9.7	6.4	0	93	29	21	0.3	88.1	41.5	14.2	2127693	201419	55941	9401	9.6
13	2252	2788	2509	130	3.9	15.4	5.8	2.2	0	70	18	15	0.8	84.5	41.0	12.3	2196125	80864	11781	1162	9.2
14	2682	2993	2849	87	4.0	16.1	6.3	2.3	0	68	20	14	0.2	85.6	29.2	12.7	2938209	114631	19903	2015	12.3
15	2944	3186	3059	58	3.9	17.5	6.7	3.1	0	83	21	19	0.1	83.0	26.2	10.5	1883185	153048	30433	2919	8.3

[a] "Min" denotes the minimum values of elevation, tree height, canopy cover, and slope, respectively.

[b] "Max" denotes the maximum values of elevation, tree height, canopy cover, and slope, respectively.

[c] "SD" denotes the standard deviation of elevation, tree height, canopy cover, and slope, respectively.

[d] "Return numbers" represents the number of first, second, third, and fourth returns, respectively.

151 *2.2. LiDAR data*

152 The LiDAR data used in our study were acquired as part of the National Critical
153 Zone Observatory Project in August 2010, using an Optech GEMINI airborne laser
154 terrain mapper. The acquisition was performed ~600 m above the ground with an
155 average point density of 10.27 pts/m^2. The scanning frequency was set to 50 Hz and
156 the scan angle was smaller than ±14° from nadir. The swath width of a single pass
157 was 233.3 m, and the overlap between two adjacent swaths was greater than 50%.
158 To evaluate the performance of the filtering algorithm, we generated filtered
159 reference data for each site using the standard industrial procedure. We used the
160 automatic filtering tool in software Terrascan to obtain the initial filtering results.
161 Then the manual classification tools were used to improve the initial filtering results
162 to ensure the quality of the reference data. Specifically, the DTMs generated using the
163 initial filtering results were visually checked to find irregular raised and low surfaces.
164 The corresponding point clouds were examined manually by visualizing the cross
165 section of the point clouds and the mislabeled points were corrected (Hodgson and
166 Bresnahan, 2004; Waldhauser et al., 2014). The National Agriculture Imagery
167 Program aerial imagery, acquired in 2009 with the resolution of 1 m, was overlaid
168 with the LiDAR data to assist the manual correction, especially in complex regions.
169 The manual filtering results were revised more than once to ensure accuracy. Many
170 published papers related with filtering algorithms adopted this method to generate the
171 reference data to analyze and compare the algorithms (Sithole and Vosselman, 2004;

Kobler et al., 2007; Shao and Chen, 2008; Mongus and Žalik, 2012; Guan et al.,2014).

For each site, we calculated the numbers of the manual corrected points (Table 2).

Table 2

Statistics of manually corrected points. Corrected ratio is the ratio of the number of manually corrected points (including corrected ground points and corrected non-ground points) to the total number of points.

Site	Corrected ground points	Corrected non-ground points	Uncorrected ground points	Uncorrected non-ground points	Corrected ratio(%)
1	211183	2096	1497116	881626	8.2
2	344329	652	1274714	1376533	11.5
3	11811	160546	334458	3027619	4.9
4	13849	148783	328715	3011263	4.6
5	236958	561	878898	1801137	8.1
6	295899	512	1083924	1452189	10.5
7	403896	470	1642689	730422	14.6
8	287768	766	817044	1639828	10.5
9	191030	4303	1203499	1551748	6.6
10	402201	1489	1588618	135493	19.0
11	407503	1783	929623	1680798	13.6
12	512374	999	1214342	666739	21.4
13	687046	2294	1258804	341788	30.1
14	289415	5711	1387438	1392194	9.6
15	413220	685	1285722	369958	20.0

3. Methods

The proposed IPTD filtering algorithm consists of three steps (Fig. 2).The first step uses a morphological opening operation to obtain potential ground seed points $G_{\text{potential}}$. The second step filters the potential ground seed points to obtain accurate ground seed points, G_{seeds}, and the third step densifies G_{seeds} to extract the ground points G_{result} using the iteratively densifying TIN method. An overview of the proposed method is illustrated in Fig. 3.

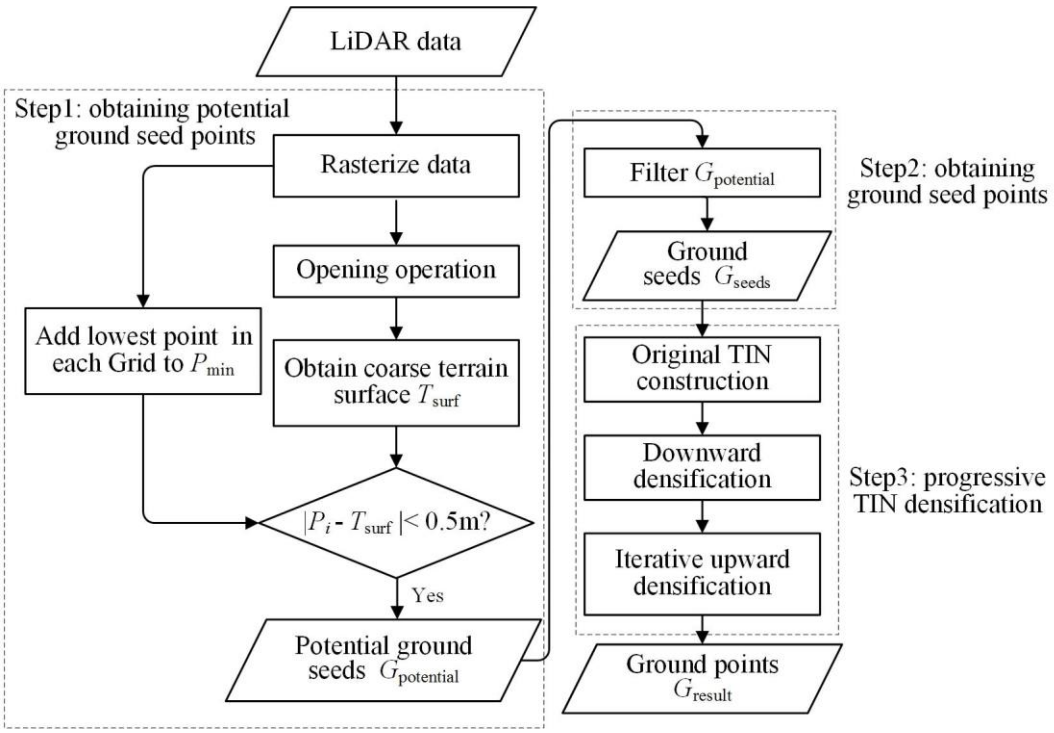

Fig.2. Flow chart of the improved progressive TIN densification filtering algorithm (IPTD), where P_{min} is the set of the lowest point in each grid and P_i is a point in P_{min}.

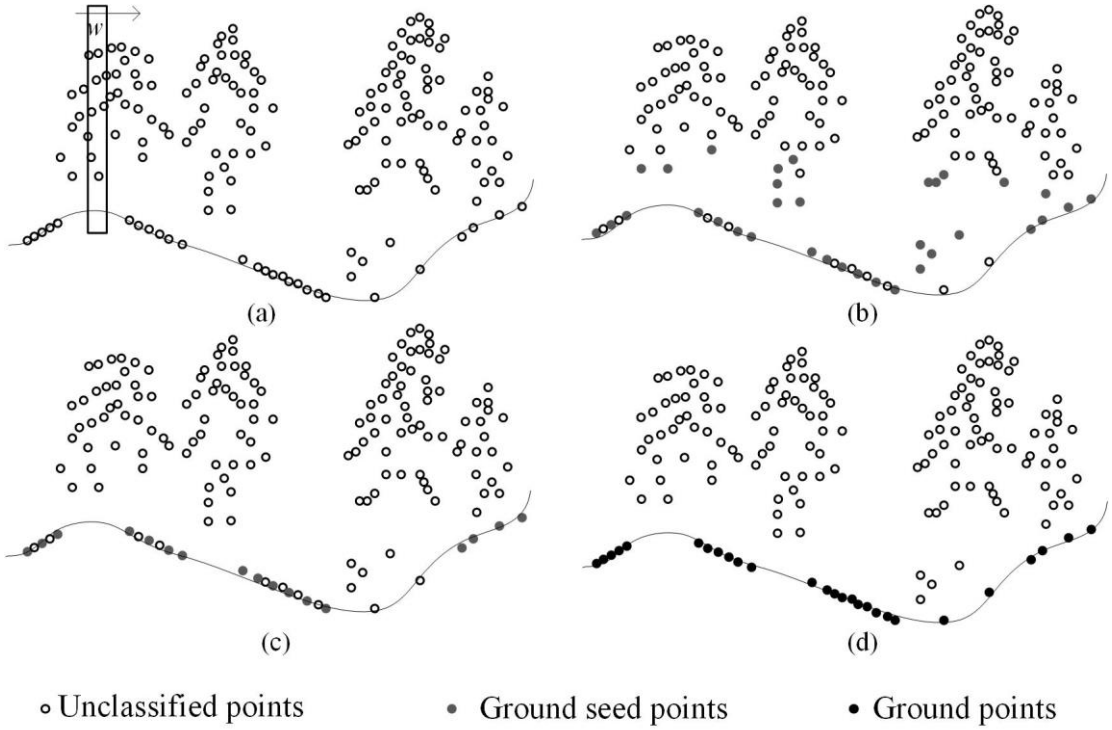

Fig. 3. Main steps in IPTD: (a) raw LiDAR data, where *w* is the structure element of the opening operation; (b) potential ground seed points (labeled with gray circles) identified using the opening operation; (c) accurate ground seed points after eliminating the non-ground points, and the eliminated non-ground points are labeled as unclassified points (labeled with empty circles); and (d) extracted ground points (labeled with black circles) using progressive TIN densification. In the final step, the remaining unclassified points are taken as non-ground points.

197 *3.1. Obtaining potential ground seed points*

198 *3.1.1. Rasterizing the point clouds*

199 Because the opening operation had to work on raster data, we must first rasterize
200 the LiDAR point clouds. The lowest point in each grid was selected to be rasterized to
201 obtain raster data P_{grid} with the grid size set to 1m in this study. The dataset P_{min}
202 recorded the lowest point in each grid for later use.

203 The sparse point density, absorptive materials on the surfaces such as water, and
204 discontinuous terrain could cause missing LiDAR data in some regions, which could
205 further produce non-data grids for $P_{grid.}$ Missing data lead to a discontinuous surface
206 and decrease the accuracy of the filtering results. To solve this problem, a binary
207 image is created where 0 represents non-data pixels and 1 represents the other pixels.
208 The morphological closing operation works on the binary image to obtain the large
209 non-data areas. Then, we could obtain the boundaries of the non-data areas by
210 subtracting the original areas from the dilated areas. Finally, the elevations of the
211 lowest cell at the boundaries are used to fill the non-data areas. The other small
212 non-data areas are filled with the elevation of its nearest cell with a value. Chen et al.
213 (2007) reported this method.

214 *3.1.2. Morphological opening operation*

215 The opening operation was applied to P_{grid} to achieve a coarse approximation of
216 the terrain surface T_{surf}. This opening operation consists of an erosion operation
217 followed by a dilation operation (Soille, 2003). Both the erosion and dilation
218 operations used the structuring element w to move along P_{grid} and probed each grid g.

For the erosion operation, the neighboring grids of g in w were searched and labeled as (x_g, y_g, z_g); the minimum value of z_g was obtained and assigned to g. The erosion result of g was the minimum value in the neighboring grids of g within w (Eq. (1)). Dilation was the opposite of erosion and the result of g was the maximum value in the neighboring grids of g (Eq.(2)). Eq.(3) gives the opening operation result of g.

$$erosion(g) = \min_{(x_g, y_g) \in w} (z_g) \quad (1)$$

$$dilation(g) = \max_{(x_g, y_g) \in w} (z_g) \quad (2)$$

$$open(g) = \max_{(x_g, y_g) \in w} (\min(z_g)) \quad (3)$$

where points (x_g,y_g,z_g) are the neighboring point set of g within window w. The window size of the structuring element for the opening operation is crucial. If the window size is too small, the terrain features are retained but some object points might remain; if the window size is too large, the vegetation points should all be removed but the terrain will also be cut down. The study sites we used were forested areas with a relatively small object size. The structuring element used was a 3 m × 3 m square.

3.1.3. Identifying potential ground seed points

The elevations of the points in P_{min} were compared with T_{surf}. If the absolute height difference was less than 0.5 m, the point was identified as a potential ground seed and added to $G_{potential}$. It is possible to filter most vegetation points while carefully retaining a large number of ground points. The following step for obtaining ground seed points can effectively eliminate the remaining vegetation points in $G_{potential}$.

3.2. Obtaining ground seed points

After application of the morphological opening operation (Fig.3b), certain non-ground points might be incorrectly included in $G_{\text{potential}}$. To eliminate these non-ground points, we used a translation plane fitting method to identify them. In $G_{\text{potential}}$, each point P_i and its nearest k points, searched using the kd-tree method (Bentley, 1990) in three-dimensional space, were used to obtain the local fitting plane F_{a} by the eigen value method (Pauly, 2003). The eigen values and eigen vectors are calculated using covariance analysis. The eigenvector corresponding to the minimum eigen value is the normal vector of the fitting plane. Because most of non-ground points are removed, the distribution of non-ground points in $G_{\text{potential}}$ is scattered and the elevations vary greatly. F_{a} could be a poor fitting plane or the distance between P_i with F_{a} could be large relatively if P_i is a non-ground point. Both situations lead to a large r, which is calculated using the k points and plane F_{b} by Eq. (4). F_{b} is a new translational plane achieved by moving F_{a} in parallel to make it pass through P_i. If r is greater than the threshold, point P_i has much chance to be a non-ground point and is deleted from $G_{\text{potential}}$. The remaining points in $G_{\text{potential}}$ are added to the ground seed points G_{seeds}.

$$r = \sqrt{\frac{\sum_{i=1}^{k} (\text{dis}(P_{\text{i}}, F_{\text{b}}))^2}{k}} \tag{4}$$

where dis(P_{i}, F_{b}) is the distance of p_{i} and F_{b}.

3.3. Iterative TIN densification

As described above, the PTD algorithm developed by Axelsson (2000) densifies G_{seeds} by comparing the iterative angle and distance with the corresponding thresholds. θ is the angle of the line connecting point P_i with the nearest node of the triangle and the triangle facet, while s is the absolute value of the distance between P_i and the triangle facet (Fig. 4c). In this process, we perform two enhancements: 1) buffer zones and simulated ground points are set to eliminate the edge effort; and 2) downward densification is performed before upward densification. The details are given as follows.

3.3.1. Initial TIN-based DTM construction

G_{seeds} is used to construct the initial TIN-based DTM. To ensure that all the points will be located in the TIN, Zhang and Lin (2013) selected four corners of the study site as simulated ground points to be joined into G_{seeds} to create the TIN. However, this method generates the TIN-based DTM with long narrow triangles along the boundary (Fig. 4a). In terrain expression using the TIN model, long narrow triangles should be avoided owing to their low credibility. Additionally, because the points around the edge of the site lack neighboring points, the quality of the TIN-based DTM at the edge is poor. Moreover, these may result in cumulative errors in subsequent iterations (Li et al., 2005). To solve this problem, we set a d_1 width buffer zone to expand the data-processing region. Along the boundary of buffer zone, the simulated ground points were arranged at fixed intervals d_2, to handle the points around the edge of the site (Fig. 4b). The elevation of a simulated ground point was the same as the elevation of its nearest point in G_{seeds}. In the experiment,d_2 was set to

30 m and the simulated ground points together with G_{seeds} were used to generate the initial TIN-based DTM. The pattern of simulated ground points settles the problem of edge effects and improves the quality of the triangles in TIN. As shown in Fig. 4b, triangles with appropriate forms and features are obtained. The objective of setting a buffer zone is explained in Section 3.3.3.

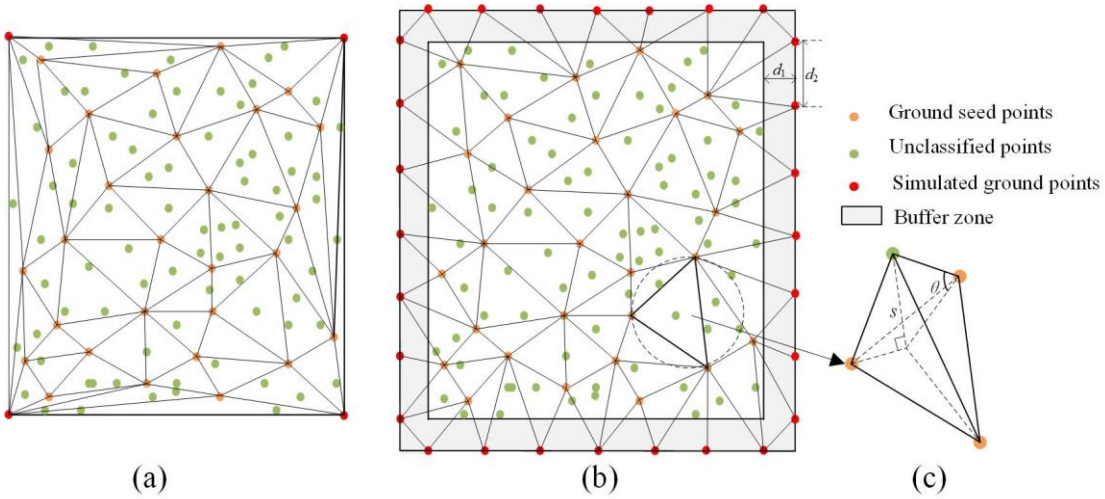

Fig. 4. (a) Original TIN-based DTM constructed using ground seed points and simulated ground seed points consisting of corners, without a buffer zone; (b) original TIN-based DTM constructed with ground seed points and simulated ground points at the boundary of the buffer zone; and (c) iterative angle θ and iterative distance s.

3.3.2. Downward densification

After the construction of the initial TIN-based DTM, the classic PTD performs upward densification directly (Axelsson, 2000). On the contrary, IPTD performs a downward densification before upward densification to improve the quality of the initial TIN-based DTM. Generally, most of the unclassified points are above the TIN while a few are below the TIN. The ground points below the TIN would be misclassified as non-ground points when the distances between them to the TIN are greater than s. These situations usually occur in low regions with trees. This step makes the initial TIN-based DTM to approximate the real terrain as much as possible

298 so the unclassified points are almost above the TIN-based DTM.

299 As shown by the example in Fig. 5, points P_3, P_4, and P_5 under the TIN facet
300 belong to the terrain, but they are unlikely to be identified as ground points because
301 the distances between them and the facet are likely to be greater than s. In contrast,
302 points P_1 and P_2 would be added to the TIN, because they are both close to it.
303 Consequently, this would create a TIN-based DTM higher than the actual ground. In
304 addition, this would also cause simultaneous misclassification of ground points and
305 non-ground points. To deal with this problem, we further investigate the points
306 beneath each triangle in the TIN. The point with the largest vertical distance to the
307 triangle facet is identified as a ground point and added to update the TIN. In Fig. 5,
308 after downward densification, P_3 joins the TIN, and the facet changes to the TIN facet
309 denoted with a dashed line. Now, P_4 and P_5 have a high probability of being classified
310 as ground points in the following step of iterative upward densification.

311

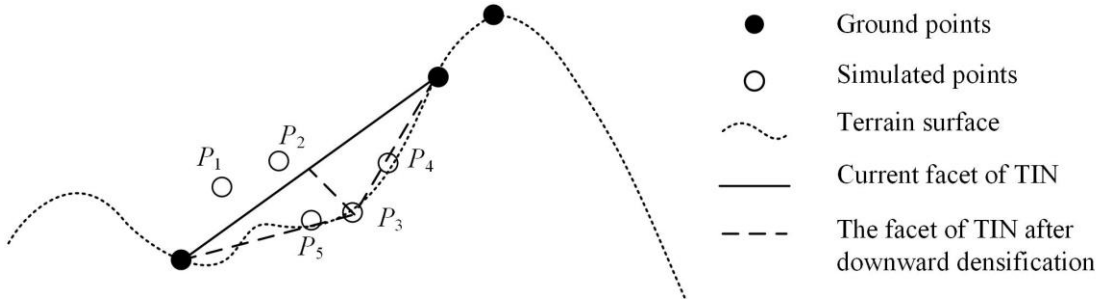

312

313 **Fig. 5.** Simple demonstration of downward densification.

314 *3.3.3. Iterative upward densification*

315 In the process of iterative upward densification, here are two iterative parameters:
316 θ and s. Unclassified points are identified as ground points when θ and s are no
317 greater than the corresponding thresholds. The detailed steps are demonstrated in Fig.

6. It should be noted that the unclassified points are sorted in ascending order by elevation because we believe that points with lower elevations satisfying the iterative criteria are more likely to be ground points. This strategy could increase filtering accuracy as TIN densification relies on a procedure for approximating the terrain from bottom to top. Iterations are terminated when no additional ground points are added to the TIN.

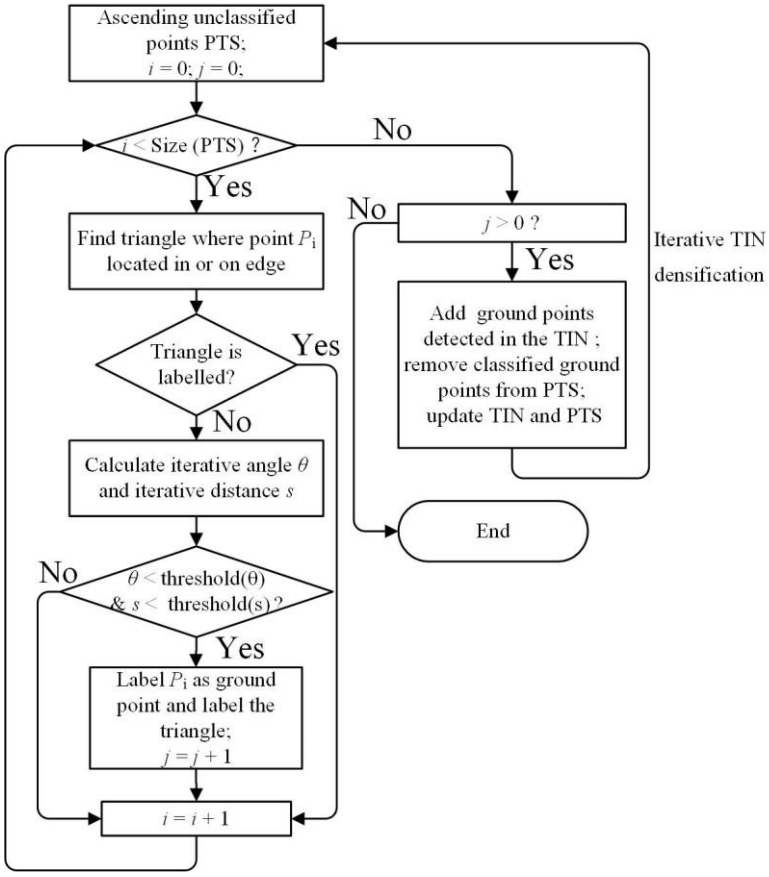

Fig. 6. Detailed flowchart of iterative upward densification. PTS denotes the ascending unclassified points; size (PTS) is the size of PTS; *i* is the index of points in PTS; *j* is the number of points added to the TIN in each iteration; threshold θ is the angle threshold, and threshold *s* is the distance threshold.

Because the simulated ground points do not actually exist, their influences in the iterative process are unexpected and should be eliminated; this is the objective of setting a buffer zone. Width $d_1$was set to 30 m in this study, which was considered to be large enough to avoid having a simulated ground point as the nearest node to an

unclassified point for our sites. For example, as shown in Fig. 7a, simulated points P_3' and P_3 are located at the edges with and without the buffer zone, respectively. Fig. 7b and 7c show the densifying procedure with triangles containing P_3 and P_3', respectively. Here, P_3 is close to P_1 and P_2, and P_3 maybe the nearest node to P_4. Values of θ in Fig. 7b may be used for comparison with the threshold. The simulated points have an impact on the determination of unclassified points. The buffer zone extends the line between P_4 and P_3', preventing P_3' from being the closest point to P_4, and avoiding the comparison between θ' and the threshold angle (Fig. 7c).

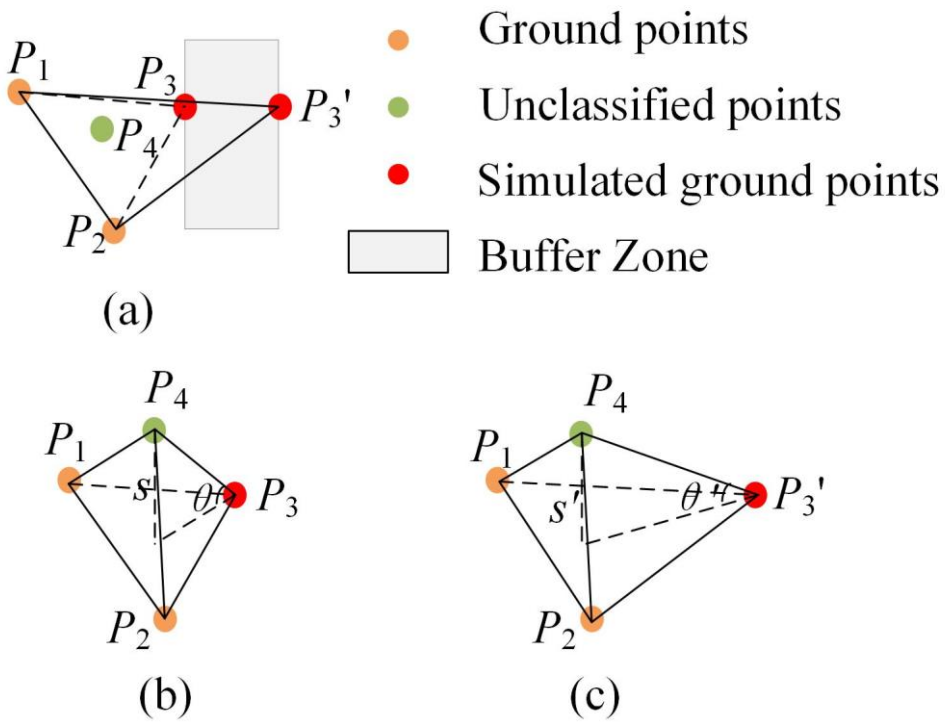

Fig. 7. Detailed illustration of buffer zone function: (a) triangles $\triangle P_1P_2P_3$ constructed using a simulated ground point P_3 not at the boundary of the buffer zone, and $\triangle P_1P_2P_3'$ constructed using a simulated ground point P_3' at the boundary of the buffer zone; (b) triangular pyramid consisting of triangle $\triangle P_1P_2P_3$ and an unclassified point P_4; and (c) triangular pyramid consisting of triangle $\triangle P_1P_2P_3$' and an unclassified point P_4.

3.4. Quantitative evaluation

We computed cross-matrices of errors, including Type I errors (*TI*), Type II

errors (*TII*), total errors (*TE*) and kappa coefficient (*kp*) to evaluate the filtering performance. The cross-matrices of errors proposed by Sithole and Vosselman (2004) are used to determine the proportion of misclassified ground points and non-ground points, while the *kp* value (Cohen, 1960) indicates the classification accuracy. The equations are given in Table 3.

Table 3

Calculation of Type I errors (*TI*), Type II errors (*TII*), total errors (*TE*), and kappa coefficients (*kp*): *a* and *b* are the numbers of ground points, respectively, classified correctly and incorrectly; *d* and *c* are the numbers of non-ground points, respectively, classified correctly and incorrectly; and *e* is the sum of *a*, *b*, *c*, and *d*.

		Filtered		Metrics of quantitative evaluations	
		Ground	Non-ground	$TI = b / (a + b)$	$P_o = (a + d) / e$
Reference	Ground	*a*	*b*	$TII = c / (c + d)$	$P_c = ((a + b) \times (a + c) + (c + d) \times (b + d)) / e^2$
	Non-ground	*c*	*d*	$TE = (b + c) / e$	$kp = (P_o - P_c) / (1 - P_c)$

Four parameters are used in the IPTD, i.e., *k*, *r*, θ, and *s*, as described above. In this section, the parameter values mentioned are the parameter thresholds. To obtain the optimum result, we set each parameter to vary within a certain range based on practical experience. The threshold *r* was varied from 0.8 m to 1.2 m with an increment of 0.2 m; the neighboring number *k* was varied from 10 to 20 with an increment of 5; the iterative distance *s* was varied from 0.2 m to 1.6 m with an increment of 0.2 m; and the iterative angle θ was varied from 6° to 30° in an increment of 2°. For each site, we tested all combinations of the four parameters, 936 tests in total, to achieve the minimum *TE* values, which were taken as the optimal results. We compared the *TE* and *kp* values of the 15 sites obtained using the IPTD and the six other filtering algorithms (Kraus and Pfeifer, 1998; Vosselman, 2000; Chen et al., 2007; Evans and Hudak, 2007; Mongus and Žalik, 2012; Pingel et al.,

372 2013). Besides these algorithms, the performance of Terrascan was also included in
373 the comparison. All results were optimized to acquire the minimum *TE* except in the
374 case of the parameter-free filtering algorithm proposed by Mongus et al. (2012).

375 *3.5. Quality evaluation*

376 We further focused on a comparison of our filtering algorithm with Terrascan to
377 explore accuracy improvements visually. We clipped a portion of the data from site 12,
378 which was found difficult to process, for visual comparison. This area is very steep
379 with sparse vegetation, with an average slope of 59.02° and a maximum slope of
380 88.64°. Furthermore, there is a cliff, which makes this terrain discontinuous.

381 **4. Results**

382 The filtering results of 15 sites were compared with their corresponding
383 reference filtering data to evaluate the performance, including quantitative assessment
384 and visual interpretation of generated DTMs.

385 Table 4 shows the *TE* of the IPTD compared with the other filtering algorithms
386 for the 15 study sites. All the filtering algorithms perform satisfactorily in most
387 regions, particularly in the less complex areas. IPTD achieves the smallest *TE* in eight
388 of the 15 sites. For the remaining seven sites, the algorithm of Pingel et al. (2013) and
389 Terrascan achieve the smallest *TE* values, and the IPTD achieves the second-best
390 results in six of these seven sites. The *TE* values of IPTD ranges from 1.32% to 5.04%.
391 Although the highest *TE* obtained in site13, our method still produces the comparative
392 best result. Additionally, our method has the lowest average *TE* and standard deviation

for all 15 study sites. The IPTD performance is also robust and stable with respect to various vegetation conditions (e.g., canopy cover and tree height) and terrain characteristics (e.g., slope and elevation) of the study sites. Even for those areas with dense vegetation on steep slopes, such as sites 11 and 12, the IPTD achieves satisfactory results with *TE* less than 5%. The results for sites with steep slopes and low vegetation, such as sites 10, 13, and 14, show large *TE* values using the other filters. However, our filter performs comparatively well in these cases.

Table 4

Comparison of IPTD *TE* values for each study site with those obtained by the other seven filtering algorithms. The bold values denote the smallest *TE* in each row, indicating the best result of all the filtering algorithms. The averages (ave) and standard deviations (sd) of the *TE* values are also shown.

	Filtering algorithm *TE* values (%)							
Site	IPTD	Terrascan	Pingel (2013)	Mongus (2012)	Evans (2007)	Chen (2007)	Vosselman (2000)	Kraus (1998)
1	3.18	**2.71**	3.48	3.77	4.51	4.03	4.60	4.84
2	**1.86**	3.78	2.87	3.02	4.57	2.93	2.81	3.70
3	4.08	**2.84**	18.33	15.68	13.64	9.75	13.61	20.74
4	4.04	**2.93**	12.35	16.84	11.88	9.55	13.35	20.35
5	**1.32**	2.59	2.22	2.28	4.13	2.77	2.94	7.60
6	**1.76**	3.63	2.28	2.34	3.98	2.98	3.14	6.09
7	**1.96**	4.67	2.21	2.33	2.89	2.23	2.21	2.75
8	**2.41**	4.14	3.09	3.36	5.81	4.98	9.38	6.00
9	3.00	**1.68**	4.75	4.84	7.12	9.66	13.68	6.92
10	3.64	6.20	**3.58**	3.97	4.93	16.3	40.03	4.08
11	**2.54**	4.39	6.00	6.71	7.60	9.33	22.95	9.52
12	**4.47**	7.82	7.47	8.27	11.35	18.36	46.56	8.88
13	**5.04**	9.16	7.66	7.70	9.05	28.75	56.44	8.15
14	4.32	**3.14**	26.02	34.73	36.46	40.10	42.97	35.37
15	3.57	7.22	**1.64**	1.71	3.87	4.97	14.55	2.71
ave	**3.15**	4.46	6.93	7.84	8.79	11.11	19.28	9.85
sd	**1.1**	2.1	6.73	8.49	8.06	10.48	17.62	8.66

Table 5 compares the accuracy of the *kp* values obtained using the IPTD and those obtained using other filtering algorithms. For the 15 study sites, the IPTD achieves the largest *kp* values in nine of the 15 study sites, exceeding those for the

other filtering algorithms. For the remaining six sites, the algorithm of Pingel et al. (2013) and Terrascan achieve the highest *kp* values, and the IPTD achieved the second-highest *kp* values in five sites. The *kp* values range from 72.77% to 97.21%. The lowest *kp* value is obtained in study site 10, nevertheless, compared with other results, this *kp* value of IPTD is the highest. Additionally, our method yields the highest averages and smallest standard deviations for *kp* values.

Table 5

Comparison of IPTD *kp* values for each study site with those obtained by the seven other filtering algorithms. The bold values denote the largest *kp* value in each row, indicating the best result of all the filtering algorithms. The average (ave) and standard deviation (sd) of *kp* values are also shown.

	Filtering algorithm*kp*values(%)							
Site	IPTD	Terrascan	Pingel (2013)	Mongus (2012)	Evans (2007)	Chen (2007)	Vosselman (2000)	Kraus (1998)
1	92.87	**94.06**	92.10	91.37	89.82	90.86	89.64	88.86
2	**96.26**	92.43	94.19	93.9	90.79	94.07	94.31	92.50
3	79.31	**84.42**	43.45	48.19	49.96	57.52	50.37	39.62
4	79.39	**83.65**	53.38	46.00	52.9	57.96	50.83	40.18
5	**97.21**	94.45	95.35	95.21	91.22	94.16	93.79	84.49
6	**96.47**	92.72	95.45	95.32	92.03	94.03	93.71	87.84
7	**94.98**	88.59	94.16	93.82	92.47	94.13	94.19	92.65
8	**94.97**	91.26	93.63	93.10	87.85	89.65	80.04	87.81
9	93.99	**96.63**	90.52	90.35	85.73	80.57	72.38	86.21
10	**72.77**	63.33	61.63	60.71	56.16	27.20	6.86	58.79
11	**94.85**	91.03	87.99	86.60	84.52	81.00	51.63	81.11
12	**89.23**	82.05	80.14	78.31	71.67	59.67	17.53	76.47
13	**80.78**	70.84	64.41	64.53	61.71	30.00	9.36	62.40
14	91.29	**93.69**	45.03	25.27	25.9	20.35	14.03	23.81
15	88.53	78.69	**94.25**	94.04	87.16	84.01	61.08	90.34
ave	**89.53**	86.52	79.05	77.11	74.66	70.35	58.65	72.87
sd	**7.48**	9.21	19.01	21.84	19.85	25.66	32.23	21.71

The optimized parameter values for the 15 sites are shown in Table 6. When the slope is large, parameter *r* should probably be set to 1.2 m, with this value changing to 0.8 m for flat areas. An iterative angle of 30° is found to be generally appropriate. The iterative distance is the only parameter that varies greatly among the sites. Based on the parameter set for the optimized results for each site, we adjusted the parameter set as follows: $k \in \{10, 15, 20\}$, $r \in \{0.8, 1.2\}$, $\theta = 30°$, and $s \in \{0.2, 0.4, 0.6, 0.8, 1.0, 1.2, 1.4, 1.6\}$.Finally, 48 results for each site were averaged. The differences between the *TE* and *kp* values for the average and optimized results are no greater than 1% and 2%, respectively, for most sites (Table 6). The average *TE* and *kp* results indicate that IPTD is robust in most cases.

Table 6

Optimized results with corresponding parameter sets, and the average results. The averages (ave) of the *TI*, *TII*, *TE*, and *kp* values are also shown.

Site	Parameter set				Optimized results (%)				Average results (%)	
	k	*r* (m)	*θ* (°)	*s* (m)	*TI*	*TII*	*TE*	*kp*	*TE*	*kp*
1	20	0.8	30	0.2	1.50	6.41	3.18	92.87	3.31	92.57
2	15	0.8	30	0.4	1.71	2.04	1.86	96.26	1.87	96.25
3	20	0.8	6	1.6	7.73	3.69	4.08	79.31	12.67	54.26
4	20	0.8	6	1.6	8.18	3.59	4.04	79.39	12.44	54.73
5	20	0.8	30	0.6	1.71	1.08	1.32	97.21	1.46	96.90
6	20	1.0	30	0.6	2.18	1.37	1.76	96.47	1.84	96.31
7	15	1.0	30	0.8	1.59	2.99	1.96	94.98	1.97	94.95
8	20	0.8	30	0.6	4.22	1.19	2.41	94.97	2.47	94.84
9	10	0.8	20	1.4	3.34	2.69	3.00	93.99	3.81	92.38
10	10	1.2	30	1.6	2.77	16.40	3.64	72.77	3.81	72.05
11	15	0.8	30	0.6	3.72	1.60	2.54	94.85	2.65	94.62
12	15	1.2	30	1.4	5.12	2.78	4.47	89.23	4.72	88.69
13	15	1.2	30	0.8	3.54	13.53	5.04	80.78	5.35	79.87
14	10	1.2	20	0.8	4.39	4.24	4.32	91.29	7.43	84.90
15	20	1.2	30	1.2	3.86	2.28	3.57	88.53	3.64	88.35
ave					3.70	4.39	3.15	89.53	4.63	85.44

Sites 3 and 4 have an obviously greater *TI* than *TII* because the average canopy cover for sites 3 and 4 is high then a few misclassified ground points give a high *TI*. At the same time, dense vegetation points lead to a small G_{seeds} set, so the increase in ground points depends on the follow-up progressive TIN densification, which has a tendency to cause high *TI* values. Sites 10 and 13 have *TII* values greater than 10%, and their typical features are steep slopes with thinned vegetation. The reasons for this may be explained as follows. First, the LiDAR points are mainly ground points in most cases, and a few misclassified non-ground points would cause a high *TII*. Second, the window size, which is 3 m in our method, would unavoidably retain object points because of the morphological trait.

The generated DTM and the cross section of point clouds of the area for quality evaluation are given in Fig. 8. Details of the comparison show that the IPTD can

preserve the ground points on hilltops and discontinuities, whereas Terrascan hardly retains the terrain features in regions with large terrain variations. The DTM in Fig. 8c is unnatural and rough, and the detailed cross-section indicates that the ground points on steep hills and break lines are classified as non-ground points (Fig. 8f). In particular, the topographic relief obtained using the IPTD is a good practical approximation of the reference data.

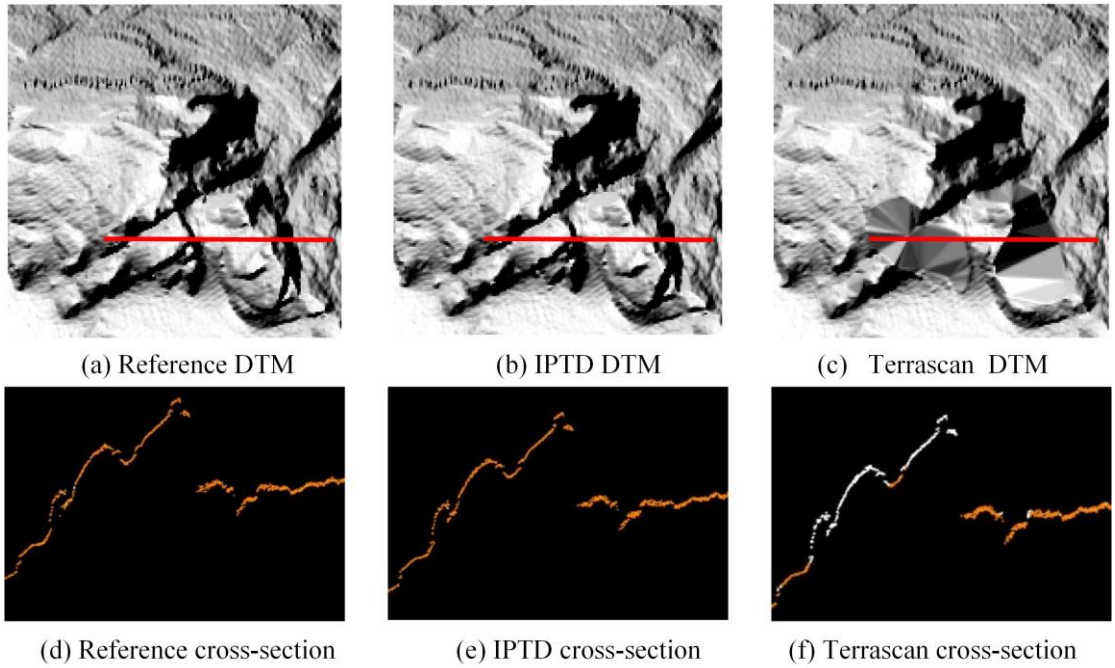

Fig. 8. Comparison of IPTD, Terrascan, and reference data with respect to the preservation of discontinuities and hilltops. Shaded relief terrain of a portion of the data from site 12 generated using (a) reference data, (b) IPTD, and (c) Terrascan. Filtering results for the cross-section indicated by the red line for (d) reference data, (e) IPTD, and (f) Terrascan. White points denote non-ground points and orange points denote ground points.

5. Discussion

5.1. Parameter analysis

Analysis of the parameter sensitivity was performed to investigate the influence of each parameter on filtering performance. We selected three typical sites, i.e., sites 5,

9, and 10, for analysis. Fig.9 shows that the change patterns of *kp* values are similar although the *kp* values are slightly different. Considering the *kp* range of each site, *k* and *r* have insignificant influences on *kp*. The reason for this may be that the distribution patterns of non-ground points for sites are similar. Another possible reason is the high-quality $G_{potential}$ that the ground points account for an extremely high proportion. For site 5 (Fig. 9a and 9b), the *kp* difference is less than 1% with the change of *s*. When *s* is lower than 0.6 m, the *kp* of site 9 decreases and *kp* of site 10 increases. While the *kp* values of site 9 and 10 remain stable when *s* is greater than 0.6 m. The suggested iterative distance of Terrascan is between 0.5 m and 1.5 m. The reason of this difference maybe that IPTD generates a large number of ground seed points that a small *s* is enough to densify TIN, even for the steep areas. That the IPTD weakens the dependence of the TIN densification on distance threshold *s* might be another reason.

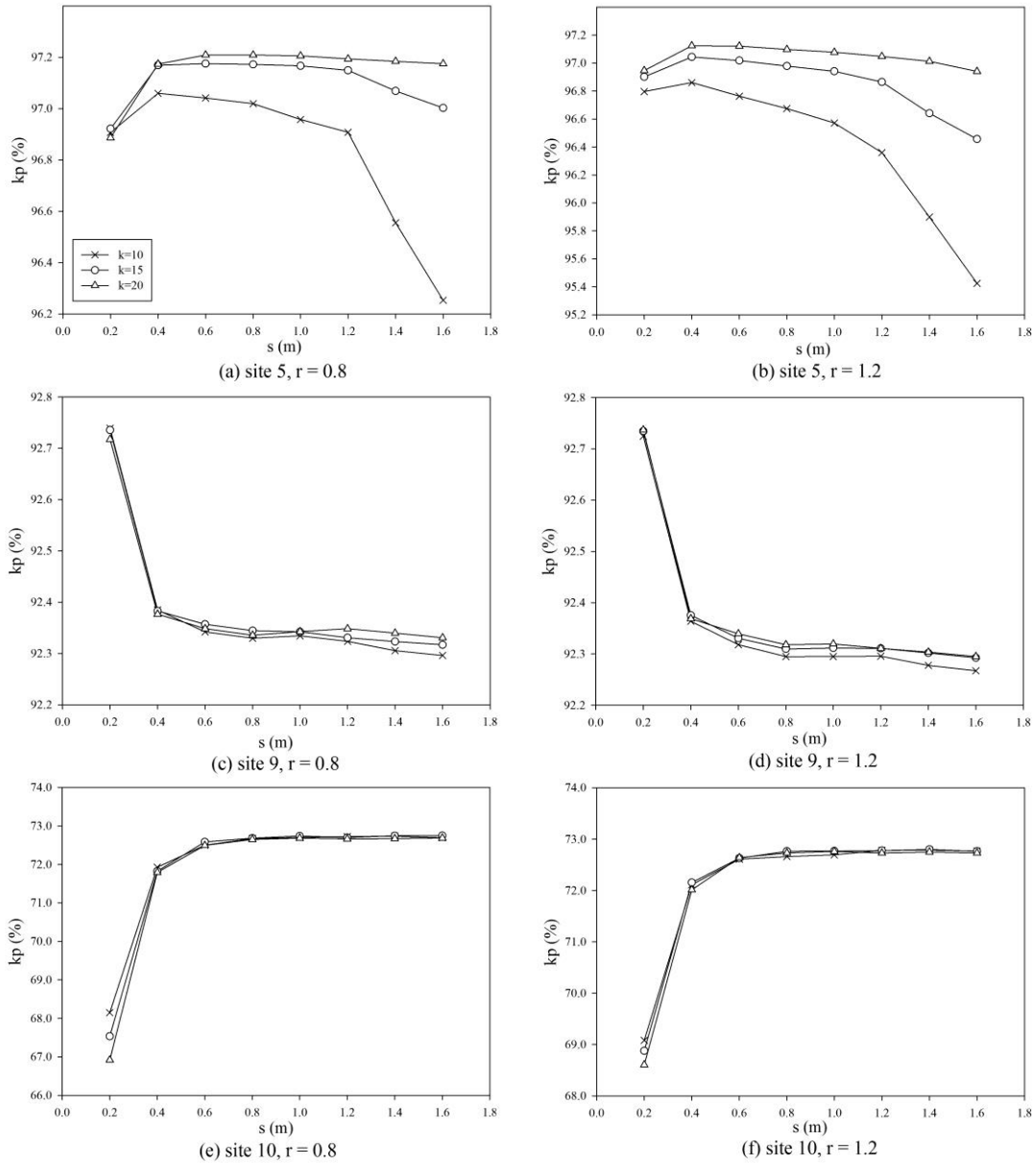

Fig. 9. Analysis of sensitivities to parameters *k*, *r*, and *s* with fixed $\theta = 30°$ for *kp* at (a) site 5, *r* = 0.8 m; (b) site 5, *r* = 1.2 m; (c) site 9, *r* = 0.8 m; (d) site 9, *r* = 1.2 m; (e) site 10, *r* = 0.8 m; and (f) site 10, *r* = 1.2 m.

k and *r* have insignificant influences on the overall performance of our method. θ and *s*, which are relatively important, are not adaptive and therefore maybe not suitable for all terrain changes. The filtering algorithms with the parameters related to the terrain or other environmental factors are usually confronted with this kind of problem. The large number of ground seed points decreases the influence of θ on the IPTD method. *s* is related with the topographic relief that for the steep regions, the *s* is

relatively higher.

5.2. Precision of ground seed analysis

To explore the effects of the steps carried out before the iterative upward densification, we computed the precision rates of $G_{potential}$, G_{seeds}, G_{down},and G_{result}. The precision rate P is calculated using Eq. (5);

$$P=a/(a+c)\times 100\% \quad (5)$$

Where P is the ratio of the number of ground points identified correctly to the number of ground points identified; a is the number of ground points classified correctly; c is the number of non-ground points that are classified as ground points incorrectly. Fig. 10 shows that the precision rates for each site increase from $G_{potential}$ to G_{seeds}, and from G_{seeds} to G_{down}. Apart from those for sites 3 and 4, which have low precision about 70%, the precisions of the other sites are about 99%. This means that the strategies we adopted not only increase the number of ground seed points, but also gradually improve the quality of the ground seed points. Because the determination of ground points is irreversible after step (2), it is vital that P of G_{seeds} is large. The final procedure, i.e., upward TIN densification, decreases all the precisions as a result of the errors caused by points misclassified as ground points. The reason may be that the distance s is not a self-adaptive threshold changing with topography variance. The performances for sites 3 and 4 are relatively poor because of the numerous errors caused by the morphological operation. It may be possible to solve this problem by enlarging the window size.

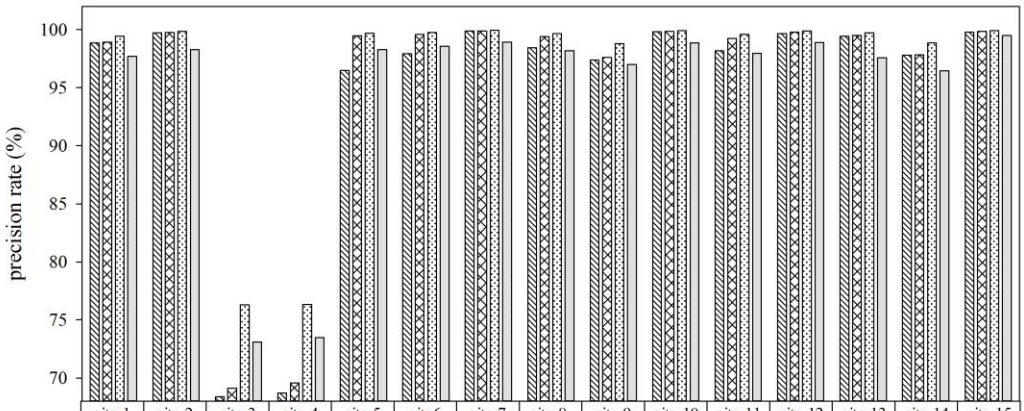

	site 1	site 2	site 3	site 4	site 5	site6	site 7	site 8	site 9	site 10	site 11	site 12	site 13	site 14	site 15
$G_{potential}$	98.85	99.73	68.38	68.71	96.47	97.91	99.89	98.44	97.38	99.82	98.16	99.66	99.43	97.79	99.79
G_{seeds}	98.91	99.75	69.14	69.57	99.47	99.58	99.89	99.39	97.61	99.84	99.24	99.78	99.49	97.84	99.83
G_{down}	99.43	99.84	76.30	76.35	99.67	99.74	99.93	99.66	98.80	99.90	99.58	99.88	99.73	98.85	99.91
G_{result}	97.69	98.27	73.10	73.48	98.26	98.55	98.93	98.19	96.99	98.85	97.96	98.88	97.58	96.43	99.48

Fig. 10. The precision rates of $G_{potential}$, G_{seeds}, G_{down},and G_{result} for 15 sites.

For very densely vegetated areas with few ground points, the accuracy could be improved by increasing the window size of the opening operation.

The classic PTD has difficulty in handling steep, rugged, and discontinuous terrains, which are common in forested areas, which has a tendency of cutting down the terrain in these areas. This situation may be caused by the sparse and uneven distributed ground seed points and the densifying process based on the ground seed points. For the classic PTD, the lowest point in each grid with a user-fixed size are selected as ground seed points, and there are no more than 100 ground seed points for our study data. While IPTD would provide more than 20, 0000 ground seed points. The morphology method could provide enough ground seed points evenly distributed in general, which enables coverage of the topographical features and retains finer details, especially for hilltops and steep slopes. The detailed changes in terrain could be presented well, especially for the areas of significantvariationsintopography. The constructed TIN based on the ground seed points are very close to the real terrain.

Moreover, a great number of ground seed points can decrease the edge effect of the TIN. In brief, the methodology method could improve the quality of initial TIN greatly which is important because the subsequent densification is based on the TIN. The great differences between the ground seed points of the two methods make the results of TIN-based densification process different. In the process of upward densification of PTD, the local slope is lack of ground seed points, and the iterative distance and angle are not adaptive with the terrain change, so it is hard to select a suitable angle threshold to keep the terrain. As shown in Figure 11, P_3, an unclassified point, is hard to be added into the terrain in the classic PTD method because of the high angle. While the IPTD that has ground seed points on the slopes, gives a solution to this situation thatP_3has a high possibility to join into the ground points.

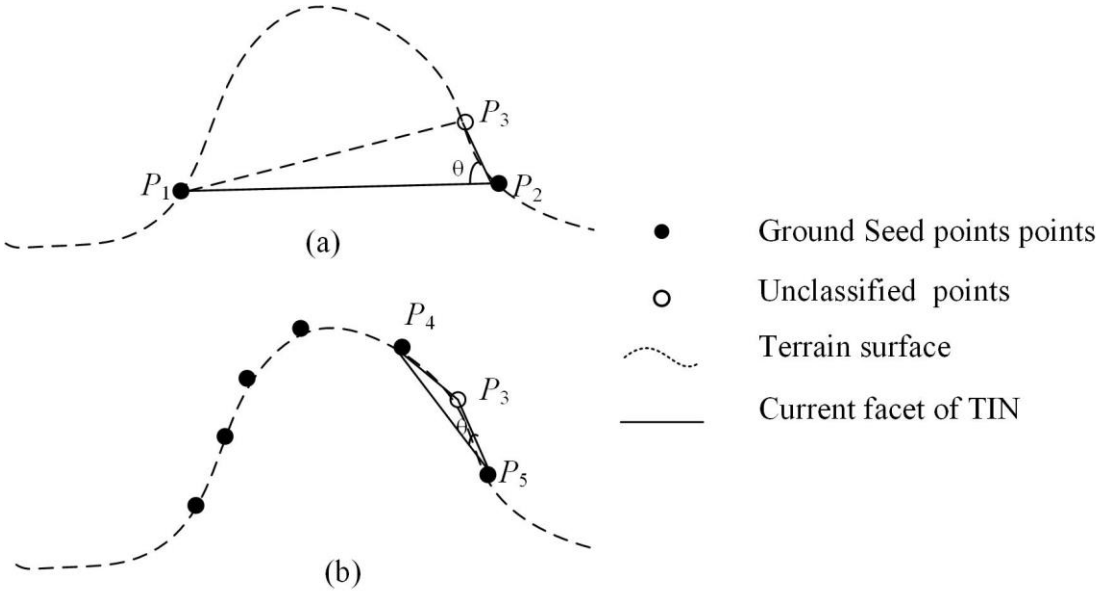

Fig. 11. The differences in upward densification for the steep areas between (a) classic PTD and (b) IPTD.

6. Conclusions

This study aims to improve the PTD method for forested areas; our results show

that the IPTD performs better than other general filtering algorithms. The strength of the IPTD lies in its ability to retain hilltops and handle break lines and steep slopes. Moreover, IPTD could be used as an efficient tool to filter airborne LiDAR data because it performs well in various forested regions. However, the IPTD has four parameters, which may influence the overall performance of the method. Therefore, future research will focus on automation of the parameterization of the algorithm, which may make the algorithm more applicable and automatic.

Acknowledgements

This research was supported by the National Natural Science Foundation of China (Grant No. 41471363). The authors would like to thank Thomas J. Pingel and Domen Mongus for generously sharing the executable programs for their algorithms.

References

Axelsson, P., 2000. DEM generation from laser scanner data using adaptive TIN models. International Archives of Photogrammetry and Remote Sensing 33, 111-118.

Bentley, J.L., 1990. K-d Trees for Semidynamic Point Sets. SCG '90: Proc. 6th Annual Symposium on Computational Geometry, 187-191.

Chen, Q., Gong, P., Baldocchi, D., Xie, G., 2007. Filtering airborne laser scanning data with morphological methods. Photogrammetric Engineering and Remote Sensing 73, 175-185.

Cohen, J., 1960. A coefficient of agreement for nominal scales. Educational and Psychological Measurement 20, 37-46.

Evans, J.S., Hudak, A.T., 2007. A multiscale curvature algorithm for classifying discrete return lidar in forested environments. IEEE Transactions on Geoscience and Remote Sensing 45, 1029-1038.

Guan, H., Li, J., Yu, Y., Zhong, L., Ji, Z., 2014. DEM generation from lidar data in wooded mountain areas by cross-section-plane analysis. International Journal of Remote Sensing 35, 927-948.

Hodgson, M.E., Bresnahan, P., 2004. Accuracy of airborne LIDAR-derived elevation. Photogrammetric Engineering & Remote Sensing 70, 331-339.

Hu, H., Ding, Y., Zhu, Q., Wu, B., Lin, H., Du, Z., Zhang, Y., Zhang, Y., 2014. An adaptive surface filter for airborne laser scanning point clouds by means of regularization and bending energy. ISPRS Journal of Photogrammetry and Remote Sensing 92, 98-111.

Kobler, A., Pfeifer, N., Ogrinc, P., Todorovski, L., Oštir, K., Džeroski, S., 2007. Repetitive interpolation: A robust algorithm for DTM generation from Aerial Laser Scanner Data in forested terrain. Remote Sensing of Environment 108, 9-23.

Korhonen, L., Korpela, I., Heiskanen, J., Maltamo, M., 2011. Airborne discrete-return LIDAR data in the estimation of vertical canopy cover, angular canopy closure and leaf area index. Remote Sensing of Environment 115, 1065-1080.

Kraus, K., Pfeifer, N., 1998. Determination of terrain models in wooded areas with airborne laser scanner data. ISPRS Journal of Photogrammetry and Remote Sensing 53, 193-203.

Li, Y., Wu, H., Xu, H., An, R., Xu, J., He, Q., 2013. A gradient-constrained morphological filtering algorithm for airborne LiDAR. Optics & Laser Technology 54, 288-296.

Li, Z., Zhu, Q., and Gold, C., 2005.Digital Terrain Modeling: Principles and Methodology. CRC Press. Boca Raton. 87-90.

Lin, X., Zhang, J., 2014. Segmentation-based filtering of airborne LiDAR point clouds by progressive densification of terrain segments. Remote Sensing 6, 1294-1326.

Liu, X., 2008. Airborne LiDAR for DEM generation: some critical issues. Progress in Physical Geography 32, 31-49.

Lucas, R.M., Cronin, N., Lee, A., Moghaddam, M., Witte, C., and Tickle, P., 2006. Empirical relationships between AIRSAR backscatter and LiDAR-derived forest biomass, Queensland, Australia. Remote Sensing of Environment, 100, 407-425.

Maltamo, M., Næsset, E., Vauhkonen, J., 2014. Forestry Applications of Airborne Laser Scanning. Springer Netherlands, 9-10.

Meng, X., Currit, N., Zhao, K., 2010. Ground filtering algorithms for airborne LiDAR data: a

589 review of critical issues. Remote Sensing 2, 833-860.
590 Mongus, D., Žalik, B., 2012. Parameter-free ground filtering of LiDAR data for automatic DTM
591 generation. ISPRS Journal of Photogrammetry and Remote Sensing 67, 1-12.
592 Müller, J., Stadler, J., Brandl, R., 2010. Composition versus physiognomy of vegetation as
593 predictors of bird assemblages: The role of lidar. Remote Sensing of Environment 114,
594 490-495.
595 Najman, L., Talbot, H., 2010.Mathematical morphology: from theory to applications, (Eds.).
596 ISTE-Wiley. 51-54.
597 Nord-Larsen, T., Riis-Nielsen, T., 2010. Developing an airborne laser scanning dominant height
598 model from a countrywide scanning survey and national forest inventory data. Scandinavian
599 Journal of Forest Research 25, 262-272.
600 Pauly, M., 2003. Point primitives for interactive modeling and processing of 3D geometry. PhD
601 dissertation. University of Kaiserslautern.
602 Pingel, T.J., Clarke, K.C., McBride, W.A., 2013. An improved simple morphological filter for the
603 terrain classification of airborne LIDAR data. ISPRS Journal of Photogrammetry and Remote
604 Sensing 77, 21-30.
605 Silván-Cárdenas, J., Wang, L., 2006. A multi-resolution approach for filtering LiDAR altimetry
606 data. ISPRS Journal of Photogrammetry and Remote Sensing 61, 11-22.
607 Sithole, G., 2001. Filtering of laser altimetry data using a slope adaptive filter. International
608 Archives of Photogrammetry Remote Sensing and Spatial Information Sciences 34, 203-210.
609 Sithole, G., Vosselman, G., 2004. Experimental comparison of filter algorithms for bare-Earth
610 extraction from airborne laser scanning point clouds. ISPRS journal of photogrammetry and
611 remote sensing 59, 85-101.
612 Sithole, G., Vosselman, G., 2005. Filtering of airborne laser scanner data based on segmented
613 point clouds. International Archives of Photogrammetry, Remote Sensing and Spatial
614 Information Sciences, 36(part 3). 66-71.
615 Soille, P., 2003. Morphological Image Analysis: Principles and Applications, 2nd Edition,
616 Springer-Verlag, New York, 203-204.
617 Susaki, J., 2012. Adaptive slope filtering of airborne LiDAR data in urban areas for digital terrain
618 model (DTM) generation. Remote Sensing 4, 1804-1819.
619 Vauhkonen, J., Packalen, P., Malinen, J., Pitkänen, J., Maltamo, M., 2014. Airborne laser
620 scanning-based decision support for wood procurement planning. Scandinavian Journal of
621 Forest Research 29, 132-143.
622 Vosselman, G., 2000. Slope based filtering of laser altimetry data. International Archives of
623 Photogrammetry and Remote Sensing 33, 935-942.
624 Waldhauser, C., Hochreiter, R., Otepka, J., Pfeifer, N., Ghuffar, S., Korzeniowska, K., Wagner, G.,
625 2014. Automated classification of airborne laser scanning point clouds. In Solving
626 Computationally Expensive Engineering Problems, 269-292. Springer.
627 Wulder, M.A., Bater, C.W., Coops, N.C., Hilker, T., White, J.C., 2008. The role of LiDAR in
628 sustainable forest management. The Forestry Chronicle 84, 807-826.
629 Zhang, J., Lin, X., 2013. Filtering airborne LiDAR data by embedding smoothness-constrained
630 segmentation in progressive TIN densification. ISPRS Journal of Photogrammetry and
631 Remote Sensing 81, 44-59.
632 Zhang, K., Chen, S-C., Whitman, D., Shyu, M-L., Yan, J., Zhang, C., 2003. A progressive

morphological filter for removing nonground measurements from airborne LIDAR data. IEEE Transactions on Geoscience and Remote Sensing, 41, 872-882.